Detection of CH3+ in the O-rich Planetary Nebula NGC 6302

The Astrophysical Journal, 995:67 (15pp), 2025 December 10 https://doi.org/10.3847/1538-4357/ae1020

Detection of CH_3^+ in the O-rich Planetary Nebula NGC 6302

Charmi Bhatt[1,2,39], Jan Cami[1,2,3], Els Peeters[1,2,3], Nicholas Clark[1], Paula Moraga Baez[4], Kevin Volk[5], G. C. Sloan[5,6], Joel H. Kastner[4,7,8], Harriet L. Dinerstein[9], Mikako Matsuura[10], Bruce Balick[11], Kathleen E. Kraemer[12], Kay Justtanont[13], Olivia Jones[14], Raghvendra Sahai[15], Isabel Aleman[16], Michael J. Barlow[17], Jeronimo Bernard-Salas[18,19], Joris Blommaert[20], Naomi Hirano[21], Patrick Kavanagh[22], Francisca Kemper[23,24,25], Eric Lagadec[26], J. Martin Laming[27], Frank Molster[28], Hektor Monteiro[29,30], Anita M. S. Richards[31], N. C. Sterling[32], Maryam Torki[23], Peter A. M. van Hoof[33], Jeremy R. Walsh[34], L. B. F. M. Waters[35,36], Roger Wesson[29,17], Finnbar Wilson[29], Nicholas J. Wright[37], and Albert A. Zijlstra[31,38]

[1] Department of Physics and Astronomy, University of Western Ontario, London, Ontario, Canada
[2] Institute for Earth and Space Exploration, University of Western Ontario, London, Ontario, Canada
[3] SETI Institute, Mountain View, CA, USA
[4] Center for Imaging Science, Rochester Institute of Technology, Rochester NY 14623, USA
[5] Space Telescope Science Institute, 3700 San Martin Drive, Baltimore, MD 21218, USA
[6] Department of Physics and Astronomy, University of North Carolina, Chapel Hill, NC 27599-3255, USA
[7] School of Physics and Astronomy, Rochester Institute of Technology, Rochester NY 14623, USA
[8] Laboratory for Multiwavelength Astrophysics, Rochester Institute of Technology, Rochester NY 14623, USA
[9] Department of Astronomy, University of Texas at Austin, Austin, TX 78712, USA
[10] Cardiff Hub for Astrophysics Research and Technology (CHART), School of Physics and Astronomy, Cardiff University, The Parade, Cardiff CF24 3AA, UK
[11] Department of Astronomy, University of Washington, Seattle, WA 98195-1580, USA
[12] Institute for Scientific Research, Boston College, 140 Commonwealth Avenue, Chestnut Hill, MA 02467, USA
[13] Chalmers University of Technology, Onsala Space Observatory, S-439 92 Onsala, Sweden
[14] UK Astronomy Technology Centre, Royal Observatory, Blackford Hill, Edinburgh EH9 3HJ, UK
[15] Jet Propulsion Laboratory, 4800 Oak Grove Drive, California Institute of Technology, Pasadena, CA 91109, USA
[16] Laboratório Nacional de Astrofísica, Rua dos Estados Unidos 154, Bairro das Nações, Itajubá, MG 37504-365, Brazil
[17] Department of Physics and Astronomy, University College London, Gower Street, London WC1E 6BT, UK
[18] ACRI-ST, Centre d'Études et de Recherche de Grasse (CERGA), 10 Av. Nicolas Copernic, 06130 Grasse, France
[19] INCLASS Common Laboratory, 10 Av. Nicolas Copernic, 06130 Grasse, France
[20] Astronomy and Astrophysics Research Group, Department of Physics and Astrophysics, Vrije Universiteit Brussel, Pleinlaan 2, B-1050 Brussels, Belgium
[21] Academia Sinica Institute of Astronomy and Astrophysics, 11F of Astronomy-Mathematics Building, AS/NTU, No.1, Sec. 4, Roosevelt Road, Taipei 106319, R.O.C., Taiwan
[22] Department of Physics, Maynooth University, Maynooth, County Kildare, Ireland
[23] Institut de Ciències de l'Espai (ICE, CSIC), Can Magrans, s/n, E-08193 Cerdanyola del Vallès, Barcelona, Spain
[24] ICREA, Pg. Lluís Companys 23, E-08010 Barcelona, Spain
[25] Institut d'Estudis Espacials de Catalunya (IEEC), E-08860 Castelldefels, Barcelona, Spain
[26] Université Côte d'Azur, Observatoire de la Côte d'Azur, CNRS, Lagrange, 96 Bd de l'Observatoire, 06300 Nice, France
[27] Space Science Division, Naval Research Laboratory, Code 7684, WA, DC 20375, USA
[28] Leidse instrumentmakers School, Einsteinweg 61, 2333 CC Leiden, The Netherlands
[29] Cardiff Hub for Astrophysics Research and Technology (CHART), School of Physics and Astronomy, Cardiff University, Cardiff CF24 3AA, UK
[30] Instituto de Física e Química, Universidade Federal de Itajubá, Av. BPS 1303, 37500-903 Itajubá, MG, Brazil
[31] Jodrell Bank Centre for Astrophysics, Department of Physics & Astronomy, The University of Manchester, Oxford Road, Manchester M13 9PL, UK
[32] University of West Georgia, 1601 Maple Street, Carrollton, GA 30118, USA
[33] Royal Observatory of Belgium, Ringlaan 3, B-1180 Brussels, Belgium
[34] European Southern Observatory, Karl-Schwarzschild-Strasse 2, D-85748 Garching, Germany
[35] Department of Astrophysics/IMAPP, Radboud University, PO Box 9010, 6500 GL Nijmegen, The Netherlands
[36] SRON Netherlands Institute for Space Research, Niels Bohrweg 4, 2333 CA Leiden, The Netherlands
[37] Astrophysics Research Centre, Keele University, Newcastle-under-Lyme, ST5 5BG, UK
[38] School of Mathematical and Physical Sciences, Macquarie University, Sydney, NSW 2109, Australia
Received 2025 June 25; revised 2025 September 16; accepted 2025 September 16; published 2025 December 4

Abstract

Planetary nebulae are sites where ejected stellar material evolves into complex molecules, but the precise physical conditions and chemical routes that govern these processes are unclear. The presence of abundant carbon-rich molecules in O-rich environments poses particular challenges. Here we report the first detection of methyl cation (CH_3^+) in any planetary nebula, observed in the O-rich nebula NGC 6302 using JWST MIRI/Medium Resolution Spectrometer observations. CH_3^+ is a key driver of organic chemistry in UV-irradiated environments. Spatially resolved observations reveal that CH_3^+ is colocated with ^{12}CO, H_2, H II, HCO^+, and polycyclic aromatic hydrocarbons. LTE modeling of the CH_3^+ emission yields excitation temperatures of 500–800 K in the inner bubble and torus, rising to 1000–2000 K in the outer bubble of NGC 6302, with column densities ranging from $\sim 10^{11}$ to 10^{13} cm^{-2}. This detection suggests that hydrocarbon radical chemistry must be incorporated into

[39] Correspondence author.

planetary nebulae chemical models. Further near-IR observations are crucial to map different chemical networks operating in these environments.

Unified Astronomy Thesaurus concepts: Small molecules (2267); Circumstellar gas (238); Astrochemistry (75); Planetary nebulae (1249)

Materials only available in the online version of record: figure set

1. Introduction

As of 2025 November, more than 340 molecular species have been identified in interstellar and circumstellar environments. A substantial subset of this inventory originates in the circumstellar envelopes of evolved stars, including stars on the asymptotic giant branch (AGB), post-AGB stars, and planetary nebulae (singular: PN; plural: PNe; B. A. McGuire 2022; M. Araki 2025). Elucidating how these molecules form and evolve as local physical conditions change is essential for constraining a wide range of astrochemical and astrophysical processes such as star- and planet formation and the chemical enrichment of galaxies, among others (see A. G. G. M. Tielens 2013 for a review).

During the AGB phase, low- to intermediate-mass ($\sim$1–8 $M_{\odot}$) stars undergo severe mass loss with mass-loss rates ranging from 10^{-8} to 10^{-4} $M_{\odot}$ yr^{-1} (S. Höfner & H. Olofsson 2018). These AGB outflows result in the formation of a circumstellar envelope (CSE). As the stellar gas expands radially away from the stellar atmosphere, it cools down, resulting in the formation of molecules and dust. The infrared (IR) spectra of AGB stars indeed show the presence of a rich variety of molecules. More than 90 molecules have been detected in the CSE around carbon-rich stars, and about 27 around oxygen-rich stars (see M. Agúndez et al. 2014; L. Decin et al. 2018; M. Agúndez 2022; B. A. McGuire 2022, and references therein). Note that the molecular species detected in the CSE of AGB stars are mainly simple molecular species, such as CO, C_2H_2, HCN, CO_2, H_2O, etc. Eventually, the star progresses through the post-AGB phase, and the effective temperature of the star, $T_{\rm eff}$, increases rapidly with decreasing stellar radii. As $T_{\rm eff} \gtrsim 20{,}000$ K, UV radiation from the star ionizes the hydrogen in the previously ejected material, and a PN is formed (K. B. Kwitter & R. B. C. Henry 2022). UV photons from the star can also lead to dissociation of molecules in the CSE, and not all molecules survive the transition from the AGB to the PN phase. In fact, a sharp drop is seen in the molecular inventory of PN compared to that of the AGB phase (M. Agúndez 2022). Interestingly, spectral features of larger and more complex molecules like polycyclic aromatic hydrocarbons (PAHs) and fullerenes, such as C_{60} and C_{70}, begin to appear in the post-AGB and PN phase (M. Matsuura et al. 2005, 2014; J. Cami et al. 2010; Y. Zhang & S. Kwok 2011; N. L. J. Cox et al. 2016).

A key concept in the chemistry of evolved stars is that the chemistry in the AGB outflows depends primarily on the C/O ratio of the stellar photosphere. All stars start their lives as oxygen-rich (C/O $<$ 1) stars, but third dredge-up events in low- and intermediate-mass stars ($\sim$1.5–4 $M_{\odot}$; D. A. García-Hernández et al. 2013) elevate this C/O ratio above unity late in the AGB phase, converting the envelope to carbon-rich. After H_2, the next molecule to form in the stellar photosphere is carbon monoxide (CO), which is a highly stable molecule. CO locks up all the free carbon or oxygen atoms—depending on which species is most abundant—leaving the remaining carbon or oxygen to drive further chemistry. Oxygen-rich stellar envelopes thus exhibit the presence of oxides (such as H_2O, SO, AlOH, etc.), and crystalline silicates (R. J. Sylvester et al. 1999; J. Cami 2002; T. Posch et al. 2002; L. Decin et al. 2010; H. Kim et al. 2010; E. De Beck et al. 2013; L. Decin et al. 2018) while carbon-rich stellar envelopes are characterized by the presence of hydrocarbons, PAHs, fullerenes, and amorphous dust (T. I. Hasegawa & S. Kwok 2001; J. Cami et al. 2010; M. Agúndez et al. 2014).

However, A. A. Zijlstra et al. (1991) presented the first evidence of mixed or dual chemistry in a PN, where the spectrum of a young PN (IRAS 07027-7934) showed the simultaneous presence of strong PAH emission as well as 1.6 GHz OH maser line emission. Using observations by the Infrared Space Observatory, more cases of dual chemistry in PNe were reported by L. B. F. M. Waters et al. (1998a, 1998b) and M. Cohen et al. (2002). Furthermore, using Spitzer observations, J. V. Perea-Calderón et al. (2009) showed that out of 26 PNe observed toward the galactic bulge, 21 showed signatures of dual chemistry. A larger survey by L. Stanghellini et al. (2012) showed that 46% of the bulge PNe and 24% of the galactic PNe exhibit dual chemistry. It is not clear whether this dual-chemistry phenomenon arises on the AGB or emerges later as a result of processing during the PN phase. Consequently, our knowledge and understanding of the chemical pathways in late stages of stellar evolution, from the AGB phase to PN, is incomplete. It is important to explore how the inventory of molecules is affected by the dual chemistry, and eventually, what chemical reactions can occur that are not accounted for by strictly C-rich or O-rich chemical pathways. This can potentially provide clues to the formation of other chemical species; for example, the formation of large carbonaceous aromatic molecules like PAHs in an O-rich environment.

In this paper, we report the unambiguous detection of the methyl cation (CH_3^+) in the NGC 6302, a small but important carbonaceous species in what is very clearly an O-rich environment (C/O $\approx$ 0.5; N. J. Wright et al. 2011). While CH_3^+ has long been considered a key species for carbon chemistry in interstellar environments (J. H. Black & A. Dalgarno 1977; D. Smith 1992; A. Sternberg & A. Dalgarno 1995; E. Herbst 2021), its first detection outside the solar system is a much more recent milestone. CH_3^+ was first detected via JWST/MIRI observations of the irradiated proplyd d203-506 in the Orion Bar by O. Berné et al. (2023). The species is also present at much larger scales in the Orion Bar photodissociation region (PDR) (M. Zannese et al. 2025) and in the disk of a T Tauri star (T. Henning et al. 2024). Our detection in NGC 6302 is the first time this species has been detected in a planetary nebula.

2. Observations and Data Reduction

We use the JWST MIRI/Medium Resolution Spectrometer (MRS) observations of NGC 6302, which were obtained as

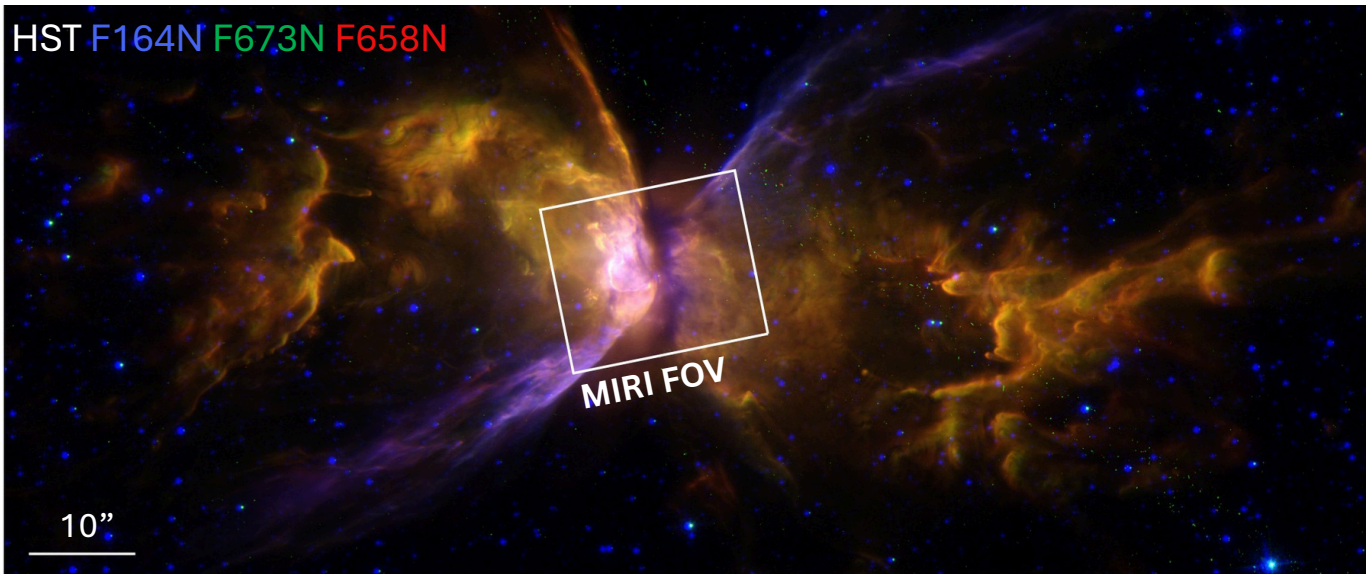

Figure 1. Three-color composite HST image of NGC 6302, created by M. Matsuura et al. (2025, MNRAS, submitted) utilizing images from J. H. Kastner et al. (2022) and B. Balick et al. (2023). This image presents a color overlay of WFC3 observations of NGC 6302, featuring F164N filter in blue, which traces [Fe II] emission, F656N filter in green, which traces Hα emission, and F658N in red, which traces [N II] emission. The white box at the center represents the MIRI field of view for observations described in Section 2.

part of the JWST GO Cycle 1 program 1742. The pointing was centered on the central region of NGC 6302 at R.A. = 17^{h}:13^{m};$44\overset{s}{.}3938$, decl. = $-37°$:06′:12.36 (J2000). The observations were taken with the MIRI MRS with an integral field unit (IFU). The data were obtained for the entire MIRI wavelength range, which is 4.9–27.9 μm spread across four channels (M. Wells et al. 2015; I. Argyriou et al. 2023). A mosaic of 5×5 tiles was used to cover the central part of NGC 6302, which includes the central star, the torus, and the bright ionized line-emitting region at the innermost region of the bipolar outflow (see Figure 1). Four-point dithering was used to optimize spatial and spectral sampling throughout the field of view.

We used the development version of v1.14.0 JWST Calibration Pipeline with versions 11.17.16 and “jwst_1202.pmap” of the Calibration Reference Data System (CRDS) and CRDS context, respectively. All level 1b files were processed through `Detector1Pipeline` to obtain level 2a (rate) images. The background exposures were subtracted from the science exposures to get background-subtracted level 2a files. These were then processed through `Spec2Pipeline` (with `residual_fringe` step tuned on), followed by `Spec3Pipeline` to produce spectral cube mosaics of NGC 6302. For details on the observations and data reduction, we refer to M. Matsuura et al. 2025, MNRAS, in press.

3. The Planetary Nebula NGC 6302

NGC 6302 is a butterfly-shaped PN, 1.03 ± 0.27 kpc away from Earth (S. Gómez-Gordillo et al. 2020), toward the constellation Scorpius. N. J. Wright et al. (2011) constructed a 3D photoionization model of NGC 6302 and constrained the properties of its central star. They derived an effective temperature of 220,000 K, which explains the presence of highly ionized species such as [Mg VII] and [Si VII]. The same study yields a stellar mass of 0.73–0.82 $M_{\odot}$ (with an initial mass of about 5.5 $M_{\odot}$), and a luminosity of 14,300 $L_{\odot}$. NGC 6302 is O-rich with C/O $\approx$ 0.5 (N. J. Wright et al. 2011).

Optical images (see Figure 1) reveal two lobes of luminous gas, shaped like the wings of a butterfly. Its bipolar lobes (which stretch as far as 2.1 pc) are exceptionally bright and exhibit a rich variety of emission lines, from the far-ultraviolet to the mid-infrared (S. Casassus et al. 2000; W. A. Feibelman 2001). NGC 6302 is known for exhibiting one of the most complex morphologies seen in PNe. Optical observations (Hubble Space Telescope (HST)/wide field camera WFC3) also reveal that the two lobes, which are oriented east–west, show small-scale structures such as clumps, tails, knots, and filaments, which seem to be in azimuthally organized zones. [Fe II] emission reveals jets coming out from the central region in southeast and northwest directions, forming an S-shape (J. H. Kastner et al. 2022; B. Balick et al. 2023).

The central region of NGC 6302 comprises three major morphological structures: the *torus* (sometimes referred to as the “central dark lane” or “main ring” in previous studies), the *inner bubble* (sometimes referred to as the “inner ring” in previous studies), and the *outer bubble*. A schematic presentation of these morphological structures is provided in Figure 2.

The torus is massive and dense with a total (dust and gas) mass of 0.8–3 $M_{\odot}$ and a size of 5700 au (M. Matsuura et al. 2025, MNRAS, in press). It is the primary reservoir of dust in NGC 6302. These authors point out that the torus is distorted or warped at the edges and is filled with crystalline silicates and other dust grains. In optical observations, the torus appears as a central dark lane that bisects the two lobes and runs nearly north–south, orthogonal to the lobes (see Figure 1). That dark lane is the front part of the torus that surrounds the central star, obscuring the star in the visible and near-IR (J. H. Kastner et al. 2022). Atacama Large Millimeter/submillimeter Array ^{12}CO $J = 3$–2 maps reveal the torus in great detail and provide kinematic information. The torus is non-Keplerian and is radially expanding at a velocity of 8 km s^{-1}. The kinematical age of the torus is estimated to be $\sim$5000–7500 yr (N. Peretto et al. 2007; M. Santander-García et al. 2017).

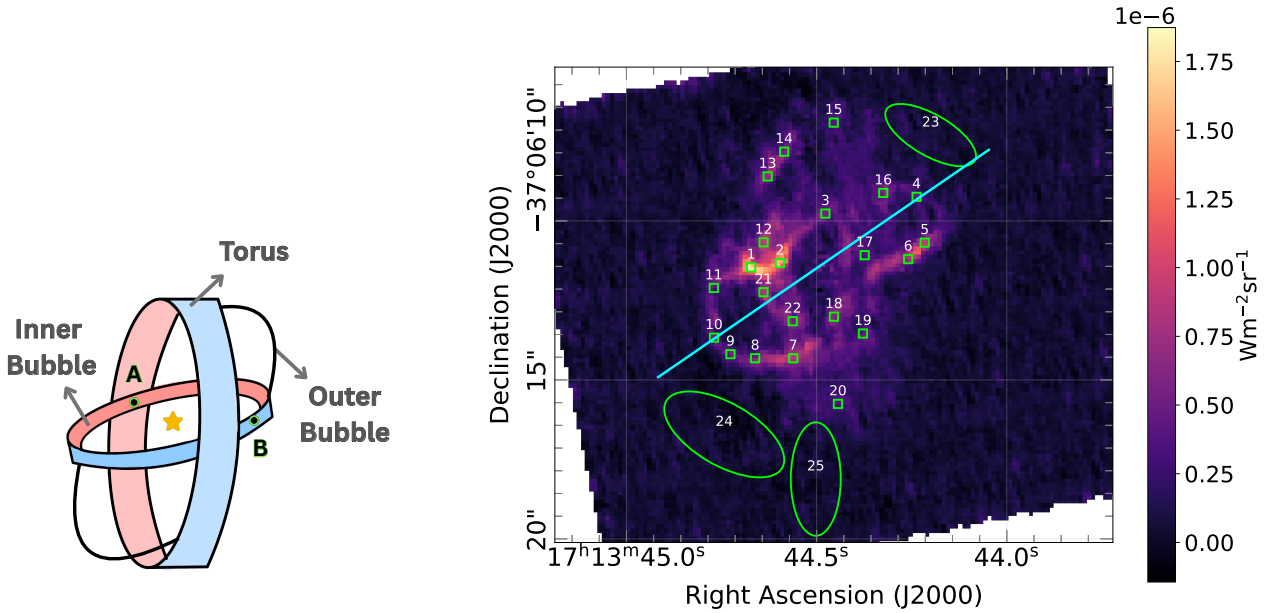

Figure 2. Left panel: the cartoon provides a schematic representation of the central region of NGC 6302. Blue and red colors indicate the blueshift and redshift caused by the expansion of the torus and inner bubble from the Earth's perspective. The schematic is based on the results of M. Santander-García et al. (2017) and M. Matsuura et al. 2025, MNRAS, in press. The line-of-sight motion of the outer bubble is not constrained and thus is represented by arcs. Points A and B are two bright spots on CH_3^+ integrated surface brightness map. Right panel: integrated surface brightness map of CH_3^+, obtained by integrating the surface brightness over the 7.13–7.2 μm wavelength range at each pixel. The green boxes and ellipses represent the 25 apertures where we analyzed the CH_3^+ emission in more detail. Apertures 1–22 are 2 × 2 pixels, which is $0\farcs26 \times 0\farcs26$. Apertures 23–25 are larger elliptical regions with areas of $3\farcs22^2$, $6\farcs52^2$, and $4\farcs36^2$, respectively. The cyan line represents the cut used for studying spatial distribution in Sec 5.

The inner bubble has been observed at optical, mid-IR, and submillimeter wavelengths as it is traced by emission of several species such as H II, H_2, ^{12}CO, HCO^+, PAHs, etc. (M. Santander-García et al. 2017; J. H. Kastner et al. 2022; M. Matsuura et al. 2025, MNRAS, in press, M. Baez et al. 2025, submitted, N. Clark et al. 2025, in preparation). The inner bubble, which runs east–west, is peanut-shaped and is pinched where it intersects with the previously ejected torus (M. Matsuura et al. 2025, MNRAS, in press). The inner bubble is inclined approximately 60° relative to the torus, and is expanding with a velocity of 11 km s^{-1}. It is much younger than the torus, with a kinematical age of ∼2200 yr (M. Santander-García et al. 2017). B. Balick et al. (2023) describe the sequence of several episodes of ejection from the center of the NGC 6302 in detail.

While the torus and the inner bubble have been detected in optical and submillimeter observations before, JWST MIRI observations by M. Matsuura et al. 2025, MNRAS, in press, revealed two arcs outside the inner bubble, toward the southeast and northwest, inclined with respect to both the inner bubble and the torus (see Figure 2). Those arcs constitute the outer bubble, which is bright in H_2 and PAH emission. (M. Matsuura et al. 2025, MNRAS, in press; Clark et al. 2025, in preparation).

4. CH_3^+ Emission in NGC 6302

The JWST/MIRI observations of the central region of NGC 6302 reveal the characteristic CH_3^+ emission band in the 7.13–7.20 μm range (see Figure 3) and show that the emission is spatially extended and resolved across distinct regions.

4.1. The Spatial Distribution of CH_3^+

To reveal the spatial distribution of CH_3^+, we integrated the surface brightness over the wavelength range 7.13–7.20 μm after continuum subtraction for each spatial pixel in the MIRI field of view. We restricted the integration to these wavelengths to avoid contributions from other species. An example of the adopted continuum is shown in Appendix A, and the resulting map of the integrated surface brightness is shown in Figure 2. The map shows bright CH_3^+ emission along the inner bubble's edge (east–west orientation) and the torus (north–south orientation). Although not visible on the map, we found that CH_3^+ is also present in the outer bubble (see below), but the column densities are too low to be visible in the integrated surface brightness map. To guide the reader and facilitate spatial comparison, we compared the CH_3^+ map to the HST/WFC3 image (through the F656N filter; see

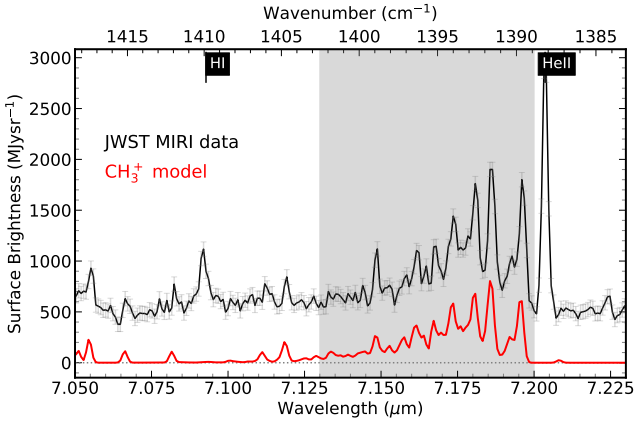

Figure 3. The continuum-subtracted JWST/MIRI spectrum of NGC 6302 at aperture 1, shown in Figure 2 (black, offset vertically for clarity), compared to a CH_3^+ model (red) by P. B. Changala et al. (2023) at an excitation temperature of 600 K. The H I recombination line at 7.0928 μm and the He II line at 7.2036 μm are labeled at the top.

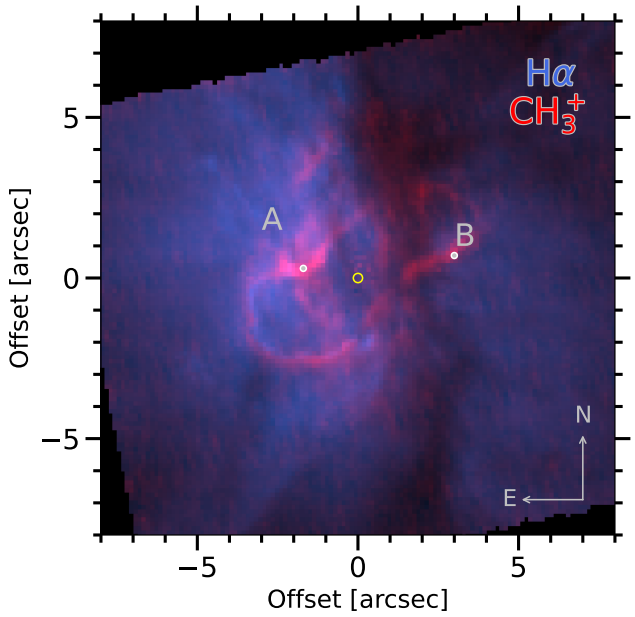

Figure 4. The image represents a color overlay of HST/WFC3 observations featuring filter F656N in blue (J. H. Kastner et al. 2022), which traces emission from Hα, and the CH_3^+ map in red.

J. H. Kastner et al. 2022), which traces Hα emission, in Figure 4. Note that the CH_3^+ emission along the torus overlaps with what appears as a central dark lane in the Hα observations.

To better understand what drives the CH_3^+ emission, we investigate its spectroscopic characteristics and spatial variations using defined apertures rather than individual pixels to achieve better signal-to-noise ratios (S/Ns). We selected 25 apertures to sample all distinct regions with CH_3^+ emission along the torus, inner bubble, and outer bubble (see Figure 2). Apertures 1–22 use 2×2 pixel areas, each covering $0\farcs26 \times 0\farcs26$ given the $0\farcs13$ pixel scale in channel 1 c. Apertures 23–25 are larger elliptical regions (with areas $3\farcs22^2$, $6\farcs52^2$, and $4\farcs36^2$, respectively) to achieve an adequate S/N for the weaker CH_3^+ emission in the outer bubble. These apertures were positioned to cover the outer bubble arc structure as guided by the H_2 map (see Appendix B). The aperture distribution is as follows: apertures 1–2 cover the intersection of the inner bubble and torus; apertures 3–6 and 7–11 trace the west and east edges of the inner bubble, respectively; aperture 12 lies north of the intersection point; apertures 13–15 trace the north rear side of the torus; apertures 16–20 and 21–22 trace the front and rear edges of the torus, respectively; and apertures 23–25 sample the outer bubble's northwest arc and south–southwest region.

4.2. Spectroscopic Analysis of the CH_3^+ Emission

CH_3^+ has a trigonal planar geometry (D_{3h} point group) and it lacks a permanent dipole moment. Because of that, it cannot be observed at radio wavelengths. However, it can be detected via rovibrational transitions at infrared wavelengths. CH_3^+ has symmetric (ν_1) and degenerate asymmetric (ν_3) stretching modes at around 3 μm ($\sim$3100 cm^{-1}), an out-of-plane umbrella bending mode (ν_2), and a degenerate in-plane (ν_4) bending mode at 7.2 μm ($\sim$1400 cm^{-1}; J. Meisner et al. 2019; P. B. Changala et al. 2023). Coriolis interactions between the ν_2 and ν_4 bands (also referred to as ν_2/ν_4 dyad) result in a characteristic pattern of rovibrational lines that occur in the 7.15–7.2 μm range.

We compare the observations to the CH_3^+ model developed by P. B. Changala et al. (2023) using the latest and most detailed rovibrational assignments of the CH_3^+ feature based on theoretical and experimental studies. They performed detailed quantum mechanical calculations to derive spectroscopic constants (for the ν_2/ν_4 dyad) such as rotational constants, coriolis coupling constant, centrifugal distortion constants, etc., in the vibronic ground state of CH_3^+. These constants were then validated by two different experimental methods. We use the `PGOPHER` (a general-purpose software for simulating electronic, vibrational, and rotational spectra; C. M. Western 2017) file provided by P. B. Changala et al. (2023) to compute the CH_3^+ model spectrum that can be compared to the observations at 7.2 μm at JWST's resolution. Note that the models assume a thermal distribution across rotational levels at the $\nu = 1$ level. We used `PGOPHER` to calculate CH_3^+ models spanning the temperature range from 100 to 3000 K in steps of 50 K, where the spectrum is convolved with a Gaussian adopting a full width half-maximum (FWHM) of 0.37 cm^{-1}, corresponding to the JWST resolving power of $R = 3600$ at 7.2 μm (channel 1c; see I. Argyriou et al. 2023). We exported the models in units of Watts per molecule.

Figure 5 shows how the Q-branch of the CH_3^+ model spectrum changes as a function of excitation temperature. At JWST's resolution, overlapping Q-branch lines cause a bump to appear. Note that the strength of different bands peaks at different temperatures based on the rotational levels of the transitions involved. For example, the strength of the 7.15 μm band is lower than that of the 7.2 μm band at lower temperatures. However, at temperatures above 1000 K, the opposite is true. The intensity ratio of the 7.15 μm band (shaded blue in Figure 5) to the 7.20 μm line (shaded red) is very small (<1) at low temperatures, $\sim$1 at about 1300 K, and much higher (>1) at high temperatures. This band ratio is thus a sensitive diagnostic of the CH_3^+ excitation temperature.

We will use this as a first estimate to determine the excitation temperature in the selected apertures, a diagnostic first used by M. Zannese et al. (2025) for the analysis of CH_3^+ emission in Orion Bar PDR. We fit a Gaussian with a linear baseline to the 7.15 μm (7.147–7.151 μm) band and 7.20 μm (7.195–7.199 μm) band, for both models and observations. The ratio of I(7.15 μm)/I(7.2 μm) derived from the model spectra versus excitation temperature is shown in Figure 6, which exhibits the behavior described above. This ratio should change gradually as a function of temperature, and to obtain a continuous form of this function, we fitted a polynomial to the data points. We found that a fifth-order polynomial fits the individual points well (see Figure 6) using the following coefficients:

$$T(x) = 1883x^5 - 7260x^4 + 10640x^3 - 6956x^2 + 2941x + 159.6, \quad (1)$$

where x is the band ratio. We can then use this polynomial to determine the excitation temperature using measured band ratios in the observational spectra. For each of the 25 apertures, we applied the same fitting procedure to the 7.15 and 7.20 μm bands as done for the models. These fits are shown in Appendix C, and the intensity and uncertainties on

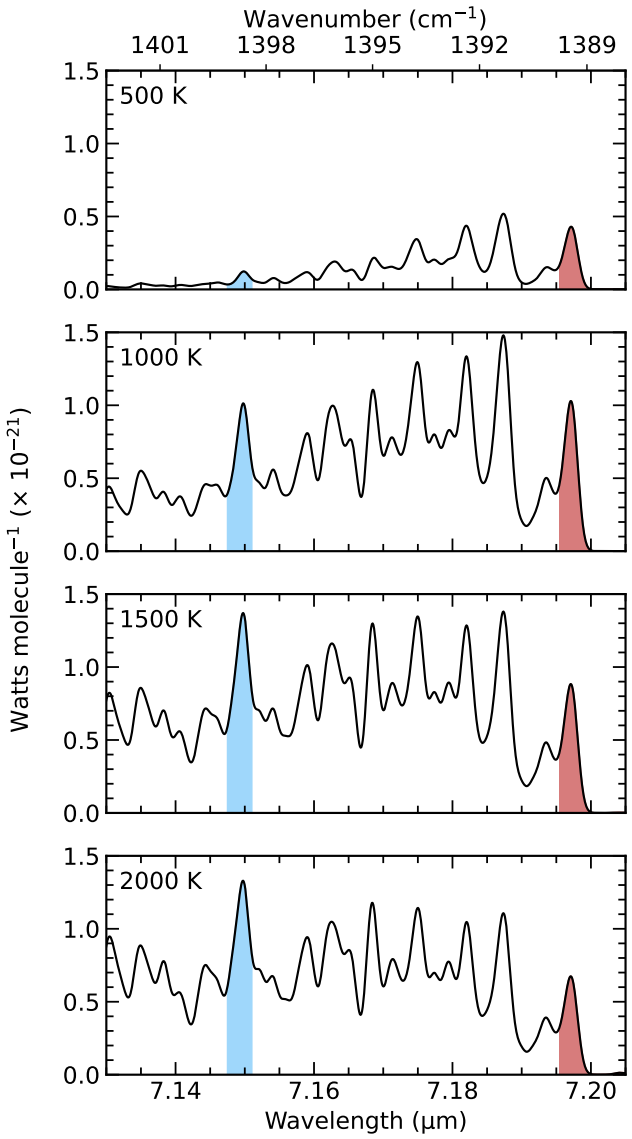

Figure 5. Model spectra of CH_3^+ at 500, 1000, 1500, and 2000 K. Bands at 7.15 and 7.2 μm are highlighted in blue and red, respectively.

the bands and the band ratios are listed in Table 1. The uncertainties in the observations determine uncertainties in the intensity. The teal points in Figure 7 show the band ratio and temperatures derived for each aperture based on Equation (1). All apertures exhibit excitation temperatures of 500–1000 K (band ratios of 0.15–0.80). While the reported uncertainties primarily reflect random errors, systematic effects-especially those introduced by the linear baseline fit are harder to quantify and could artificially increase or decrease the band ratios in certain apertures.

We can also determine the excitation temperatures by directly fitting model spectra to the continuum-subtracted spectra, with the temperature and column density of CH_3^+ as free parameters. We used the continuum-subtracted flux (in W m^{-2} μm^{-1}) in the range of 7.13–7.199 μm to fit models to observations. We used the `lmfit`(M. Newville et al. 2014) Python package, adopting a Levenberg–Marquardt algorithm to determine temperatures and column densities; the excitation temperatures, however, were constrained on a grid with values between 100 and 3000 K in steps of 50 K. We also allowed for small wavelength shifts

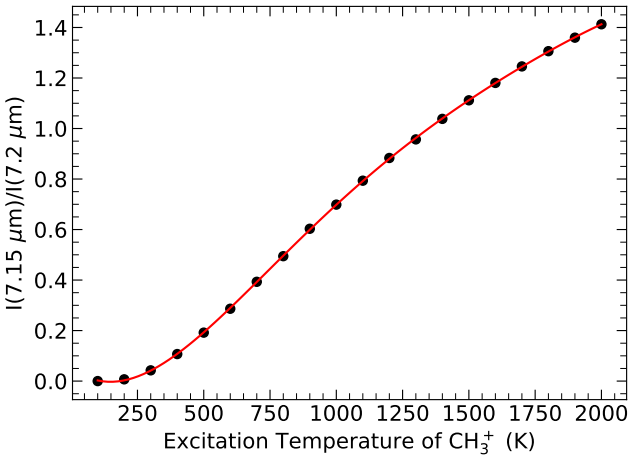

Figure 6. Intensity ratio $I(7.15\ \mu m)/I(7.2\ \mu m)$ as a function of excitation temperature of CH_3^+. Black points represent the $I(7.15\ \mu m)/I(7.2\ \mu m)$ found in the model spectra for a given excitation temperature. A five-degree polynomial fit to those points is represented by the red curve. The polynomial is given by Equation (1).

(∼±0.0015 μm) during fitting to account for radial velocity corrections. Appendix D shows the resulting best fits for all 25 apertures, and the resulting best-fit parameters are listed in Table 1. Parameter uncertainties presented in Table 1 denote 1σ confidence intervals, obtained from the projections of the $\Delta\chi^2 = 1$ contour on the χ^2 surface. The models generally reproduce the observations extremely well, leaving only very small residuals in this wavelength range. We find that the excitation temperature is in the range of 500–800 K for apertures 1–22 and temperature 1000–2000 K for apertures 23–25; these are represented by purple points in Figure 7.

Although no clear patterns exist in excitation temperature variations across the inner bubble and torus, the outer bubble exhibits significantly higher temperatures (1000–2000 K) compared to 500–800 K elsewhere. The column densities (Table 1) are typically a few times 10^{12} cm^{-2}, ranging about 2 orders of magnitude from the lowest (aperture 23) to the highest (aperture 1) values. The highest column density is seen where the inner bubble runs into the rear side of the torus. These column densities are, however, not an accurate representation of the total CH_3^+ column density, as was pointed out by O. Berné et al. (2023) and M. Zannese et al. (2025), since the CH_3^+ emission originates from chemical pumping and consequently, the excitation of the vibrational levels is far from LTE.

5. Discussion

5.1. Formation of CH_3^+ in NGC 6302

The detection of CH_3^+ in NGC 6302 was surprising at first because this is an O-rich PN where most carbon is locked up in CO, making carbon chemistry unlikely. However, intense UV radiation from the central star fundamentally changes this scenario by providing two key ingredients required for the formation of CH_3^+:C^+ ions and vibrationally excited H_2. C^+ reacts with the vibrationally excited H_2 to form CH^+, followed by two successive exothermic hydrogen abstraction reactions to produce CH_3^+ (O. Berné et al. 2023; M. Zannese et al. 2025). The UV radiation plays a crucial role because it dissociates and photoionizes CO, thereby providing C^+. Moreover, in such environments, the energy barrier of the CH^+ step (≈0.40 eV or

Table 1
The Excitation Temperature, Column Density, and Wavelength Shift for Each of the 25 Apertures from Figure 2

Aperture	$I_{7.15} \pm \sigma$ (10^{-1})	$I_{7.20} \pm \sigma$ (10^{-1})	Ratio $\pm\sigma$ (10^{-1})	T [a] (K)	T [b] (K)	$N \pm \sigma_N$ (10^{12} cm^{-2})	Wavelength Shift (10^{-3} μm)
1	8.3 ± 1.3	26.4 ± 1.3	3.1 ± 0.5	660^{+40}_{-50}	550^{+0}_{-0}	13.3 ± 0.2	−1.02 ± 0.03
2	7.2 ± 1.2	26.6 ± 1.2	2.7 ± 0.5	620^{+40}_{-50}	550^{+0}_{-50}	11.4 ± 0.2	−0.97 ± 0.04
3	4.0 ± 0.9	11.2 ± 0.9	3.6 ± 0.8	700^{+70}_{-80}	550^{+50}_{-50}	3.8 ± 0.2	−0.84 ± 0.09
4	5.5 ± 1.1	16.0 ± 1.1	3.5 ± 0.8	690^{+70}_{-70}	650^{+100}_{-100}	2.0 ± 0.1	−1.17 ± 0.1
5	4.3 ± 1.3	11.8 ± 1.3	3.7 ± 1.2	710^{+100}_{-110}	600^{+50}_{-0}	5.4 ± 0.1	−1.18 ± 0.05
6	8.9 ± 1.2	11.7 ± 1.2	7.7 ± 1.2	1110^{+150}_{-140}	550^{+50}_{-0}	5.8 ± 0.2	−1.19 ± 0.06
7	6.7 ± 0.9	15.1 ± 0.9	4.4 ± 0.7	770^{+60}_{-60}	550^{+0}_{-0}	6.9 ± 0.1	−1.16 ± 0.04
8	1.4 ± 0.9	8.6 ± 0.9	1.6 ± 1.0	490^{+120}_{-190}	550^{+50}_{-0}	4.5 ± 0.1	−1.19 ± 0.06
9	3.5 ± 1.0	12.3 ± 1.0	2.8 ± 0.9	630^{+80}_{-100}	550^{+50}_{-50}	4.1 ± 0.2	−1.12 ± 0.1
10	7.7 ± 1.2	17.7 ± 1.2	4.3 ± 0.8	770^{+70}_{-70}	500^{+50}_{-50}	5.8 ± 0.2	−1.12 ± 0.06
11	4.8 ± 1.0	6.1 ± 1.0	7.9 ± 2.0	1140^{+250}_{-220}	550^{+50}_{-50}	3.3 ± 0.2	−0.9 ± 0.1
12	0.0 ± 1.7	13.7 ± 1.7	0.0 ± 1.2	160^{+270}_{-490}	600^{+50}_{-50}	5.7 ± 0.1	−1.01 ± 0.05
13	8.0 ± 0.9	11.6 ± 0.9	6.9 ± 1.0	1020^{+110}_{-110}	550^{+0}_{-0}	5.4 ± 0.1	−0.95 ± 0.05
14	3.7 ± 0.6	10.4 ± 0.6	3.6 ± 0.6	700^{+50}_{-50}	550^{+50}_{-0}	4.5 ± 0.1	−1.1 ± 0.07
15	2.3 ± 0.9	5.4 ± 0.9	4.3 ± 1.9	760^{+180}_{-170}	850^{+100}_{-150}	1.0 ± 0.1	−0.74 ± 0.13
16	10.1 ± 0.9	12.5 ± 0.9	8.0 ± 0.9	1150^{+120}_{-110}	550^{+50}_{-0}	4.6 ± 0.2	−1.14 ± 0.07
17	4.2 ± 0.7	4.1 ± 0.7	10.2 ± 2.6	1430^{+380}_{-320}	700^{+100}_{-50}	1.4 ± 0.1	−1.13 ± 0.12
18	3.4 ± 1.2	13.6 ± 1.2	2.5 ± 0.9	600^{+90}_{-110}	550^{+50}_{-50}	4.7 ± 0.2	−1.25 ± 0.07
19	1.7 ± 0.7	4.2 ± 0.7	3.9 ± 1.7	730^{+150}_{-160}	700^{+0}_{-50}	1.8 ± 0.1	−1.34 ± 0.09
20	5.4 ± 0.8	8.6 ± 0.8	6.3 ± 1.1	960^{+130}_{-110}	600^{+50}_{-50}	2.2 ± 0.1	−1.16 ± 0.08
21	3.2 ± 0.7	10.8 ± 0.7	3.0 ± 0.7	650^{+60}_{-70}	600^{+0}_{-0}	4.8 ± 0.1	−0.81 ± 0.05
22	4.6 ± 0.9	13.5 ± 0.9	3.4 ± 0.7	680^{+60}_{-70}	550^{+50}_{-0}	4.8 ± 0.1	−0.85 ± 0.05
23	0.7 ± 0.2	1.4 ± 0.2	5.4 ± 2.1	870^{+220}_{-180}	1000^{+150}_{-150}	0.2 ± 0.0	−0.96 ± 0.11
24	1.0 ± 0.4	1.4 ± 0.4	7.0 ± 3.3	1030^{+410}_{-320}	1750^{+350}_{-150}	0.4 ± 0.0	−1.05 ± 0.1
25	0.9 ± 0.5	2.0 ± 0.5	4.4 ± 2.5	780^{+250}_{-240}	2050^{+500}_{-300}	0.4 ± 0.0	−1.05 ± 0.11

Notes.
[a] Band ratio method.
[b] Model fitting.

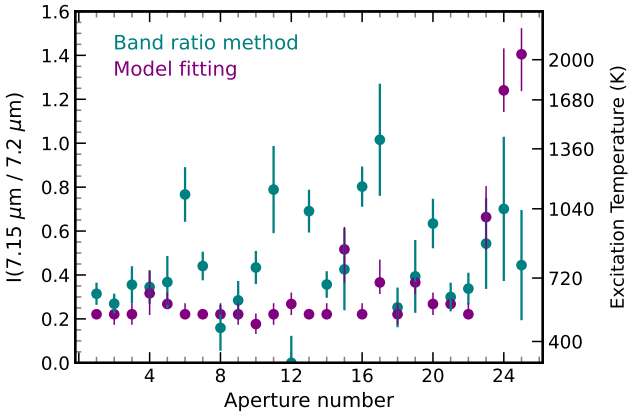

Figure 7. CH_3^+ excitation temperature derived for the 25 selected apertures. Teal points represent the $I(7.15\ \mu m)/I(7.2\ \mu m)$ band found in the observed extracted spectra. The corresponding temperatures (as described by Equation (1)) are shown on the y-axis on the right. Purple points represent the best-fit temperature derived from fitting models to the observations.

~4640 K) is overcome by far-ultraviolet (FUV)-pumped H_2, which leaves H_2 in a vibrationally excited state (M. Agúndez et al. 2010; B. Godard & J. Cernicharo 2013; Z. Nagy et al. 2013). CH^+ and CH_3^+ form in a vibrationally excited state and then relax radiatively. This excitation mechanism is called chemical (formation) pumping, and the observed emission thus traces the newly formed CH^+ and CH_3^+.

Our observations confirm this formation pathway in NGC 6302 through spatial comparison of ^{12}CO, H_2, and CH_3^+. Figure 8 shows that ^{12}CO and H_2 are indeed present where CH_3^+ emission is detected, i.e., where CH_3^+ is formed. CH_3^+ and ^{12}CO are also present in the outer bubble, but as mentioned above, their column densities are too low to be visible in the integrated surface brightness map. Since the vibrationally excited H_2 lines detected with JWST/MIRI data have very low S/N, their spatial distribution has large uncertainties for comparison with CH_3^+ distribution. We therefore use the H_2 0–0 S(5) line (at 6.908 μm) as a tracer for the H_2 distribution.

Figure 9 shows the normalized surface brightness profile of these species along the cut indicated in Figure 2, zoomed in to show the east and west edges of the bubble. On the east edge, CH_3^+, ^{12}CO, and H_2 show peaks in the surface brightness profiles at the same distance from the star, with CH_3^+ and H_2 having very similar profiles. The west edge shows a very different distribution, likely because of projection effects. Notably, CH_3^+ exhibits the sharpest rise and fall at the inner bubble edge compared to other species, including H_2. This could indicate where FUV-pumped H_2 ($v > 0$) is available; however, NIRSpec observations of vibrationally excited H_2 lines are needed for confirmation. Alternatively, this may reflect the influence of fast winds or energetic shocks that formed the inner bubble (M. Matsuura et al. 2025, MNRAS, in press), confining CH_3^+ formation to a narrow region along the edge.

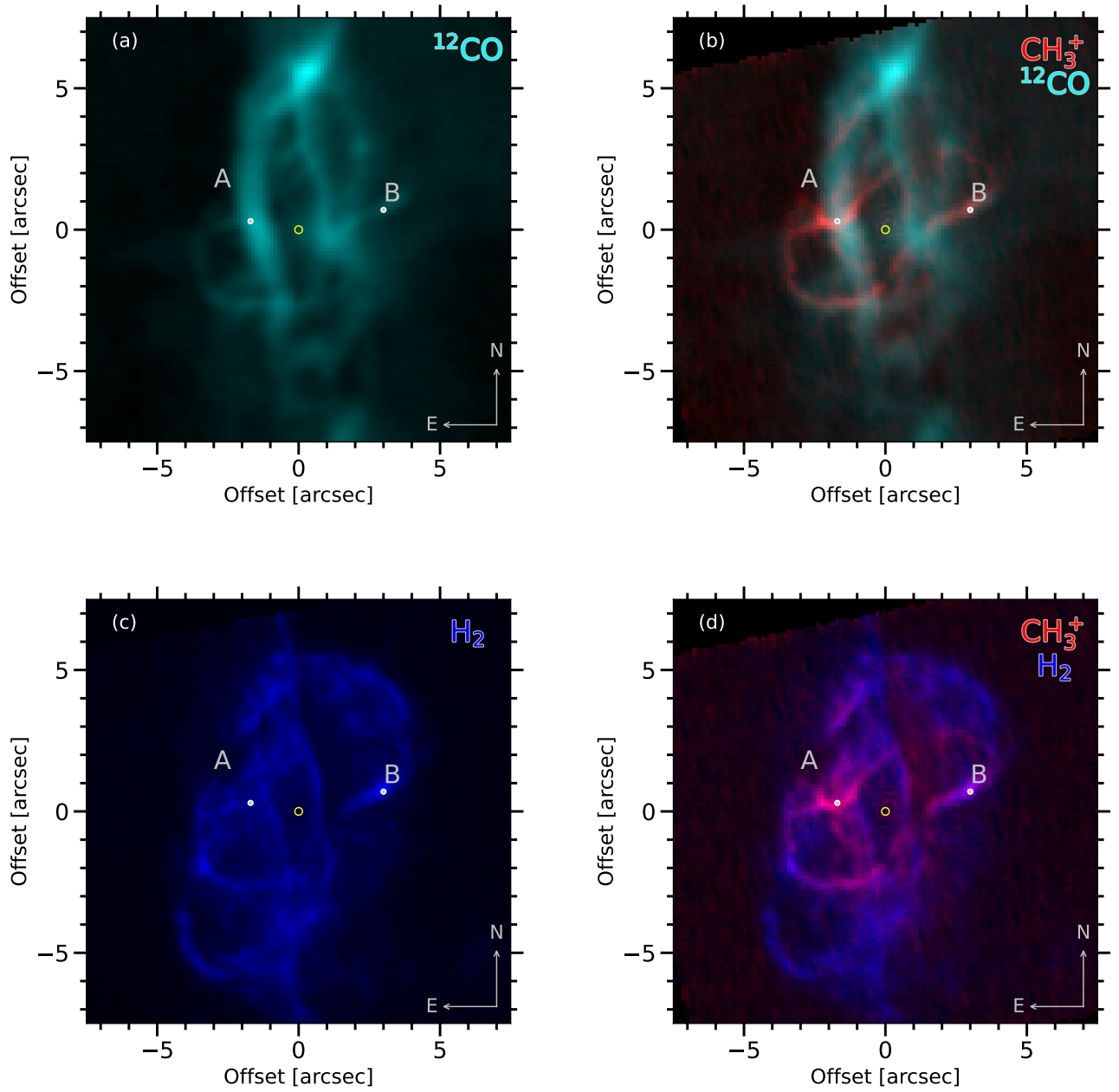

Figure 8. Comparison of the integrated surface brightness maps of CH_3^+, H_2, and ^{12}CO. (a) ^{12}CO (2–1, 230 GHz, by (b) Two color composite image: CH_3^+ (red) and ^{12}CO (cyan). (c) H_2 0-0 S5 at 6.908 μm. (d) Two color composite image: CH_3^+ (red) and ^{12}CO (cyan). Locations marked by A and B represent the two bright spots on the CH_3^+ map. The maps are centered at the central star (R.A. = 17^h:13^m:$44\overset{s}{.}488 \pm 0\overset{s}{.}004$, decl. = $-37°$:$06'$:$11\overset{''}{.}76 \pm 0\overset{''}{.}03$) whose position is indicated by the yellow circle at the center.

5.2. Spatial Variations in CH_3^+ Emission

CH_3^+ emission shows significant spatial variations in column density across NGC 6302. The most prominent features are two bright spots, points A and B, which exhibit similar temperatures to other regions but significantly higher column densities (See Figure 2). This enhancement occurs where the inner bubble runs into the torus, giving the inner bubble its characteristic peanut shape and creating regions of higher gas density. Point A (region around apertures 1, 2, and 12), exhibiting the brightest CH_3^+ emission, is located at the intersection of the inner bubble with the rear side of the torus. A corresponding bright feature is not observed where the inner bubble intersects the front side because of the extinction by the dust in the torus. However, enhanced emission is detected in both the east (aperture 7) and west (apertures 5 and 6) of this intersection, potentially tracing redirected material emerging from the intersection. This spot on the west is designated point B. Apart from higher gas density, secondary factors may also contribute to enhanced formation rates. For example, at point A, the H I emission is several times brighter than the surrounding regions, suggesting a higher UV flux, and point B coincides with a brighter H_2 emission that could boost CH_3^+ production.

In contrast, the outer bubble shows column densities 1 order of magnitude lower than typical values in the inner bubble and the torus, and 2 orders of magnitude lower than point A. This is likely due to the lower column density of CO in the outer bubble. Interestingly, the CH_3^+ excitation temperature is significantly higher in the outer bubble (1000–2000 K) than

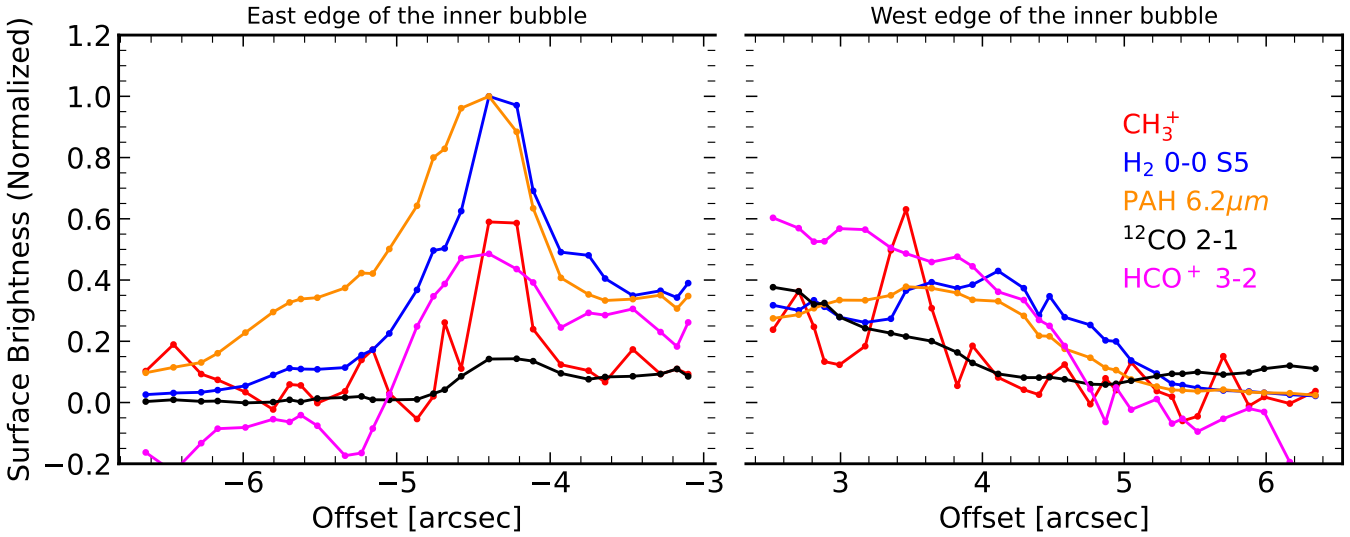

Figure 9. Normalized surface brightness profiles of CH_3^+, H_2, PAH 6.2 μm (by Clark et al. 2025, in preparation), CO, and HCO^+ (by M. Baez et al. 2025, submitted) along the cut. Offset is measured in arcsec from the position of the central star (R.A. = $17^h:13^m;44\overset{s}{.}488 \pm 0\overset{s}{.}004$, decl. = $-37°:06':11\overset{''}{.}76 \pm 0\overset{''}{.}03$).

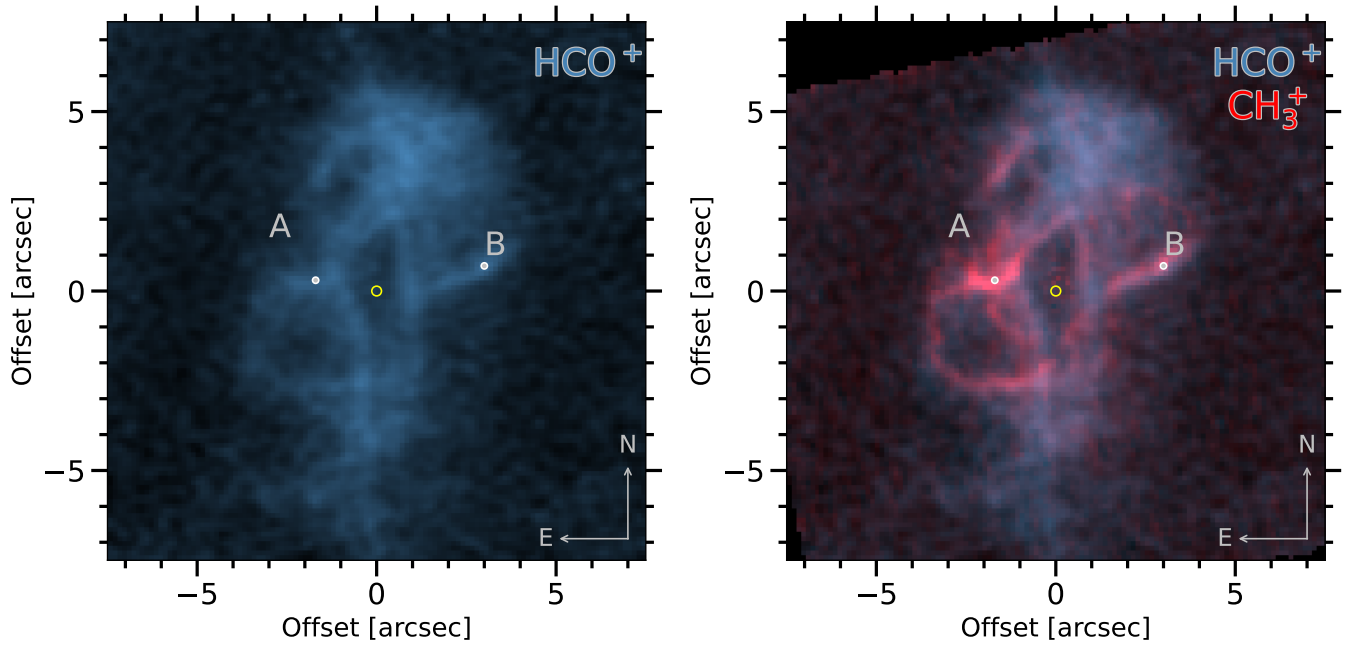

Figure 10. HCO^+ map (by M. Baez et al. 2025, submitted) is shown in blue on the left, and an overlay of the CH_3^+ map is shown in red on the right. Locations marked by A and B represent the two bright spots on the CH_3^+ map. The maps are centered at the central star (R.A. = 17:13:44.488 ± 0.004, decl. = −37:06:11.76 ± 0.03) whose position is indicated by the white circle at the center.

what is found in the inner bubble and torus (500–800 K). The chemical pumping model by M. Zannese et al. (2025) shows that higher excitation temperature of CH^+ results from enhanced H_2 level population densities, which occur when H_2 is more efficiently FUV-pumped to higher vibrational states. Similarly, hotter CH_3^+ can form if the H_2 involved in hydrogen abstraction reactions is vibrationally excited to higher levels. This indicates that the outer bubble is less shielded than the inner structures.

5.3. Chemistry Initiated by CH_3^+

The main takeaway from the CH_3^+ detection in NGC 6302 is recognizing that hydrocarbon radical chemistry, previously overlooked in oxygen-rich environments, should be incorporated into planetary nebula chemical models. CH_3^+ drives gas-phase carbon chemistry through exothermic ion-neutral reactions, with models showing it can facilitate the formation of numerous species, including CN, HCN, CH_2CO^+, CH_3OH, H_2CO, C_2H_5OH, CH_3OCH_3, H_2CN^+, etc. (see Figure 2 by D. Smith 1992 for the summary of the chemical network initiated by CH_3^+).

Spatial coincidences in NGC 6302 suggest potential connections between CH_3^+ and other observed species that warrant consideration in chemical models. CH_3^+ is spatially coincident with HCO^+ along the inner and outer bubble edges (see Figure 10), consistent with the exothermic reaction $CH_3^+ + O \rightarrow HCO^+ + H_2$ (G. B. I. Scott et al. 2000). The colocation of CH_3^+ with PAHs (see Figure 11) raises the question whether CH^+ or CH_3^+ might initiate chemistry relevant to PAH formation. M. Agúndez et al. (2008) reported that strong FUV/

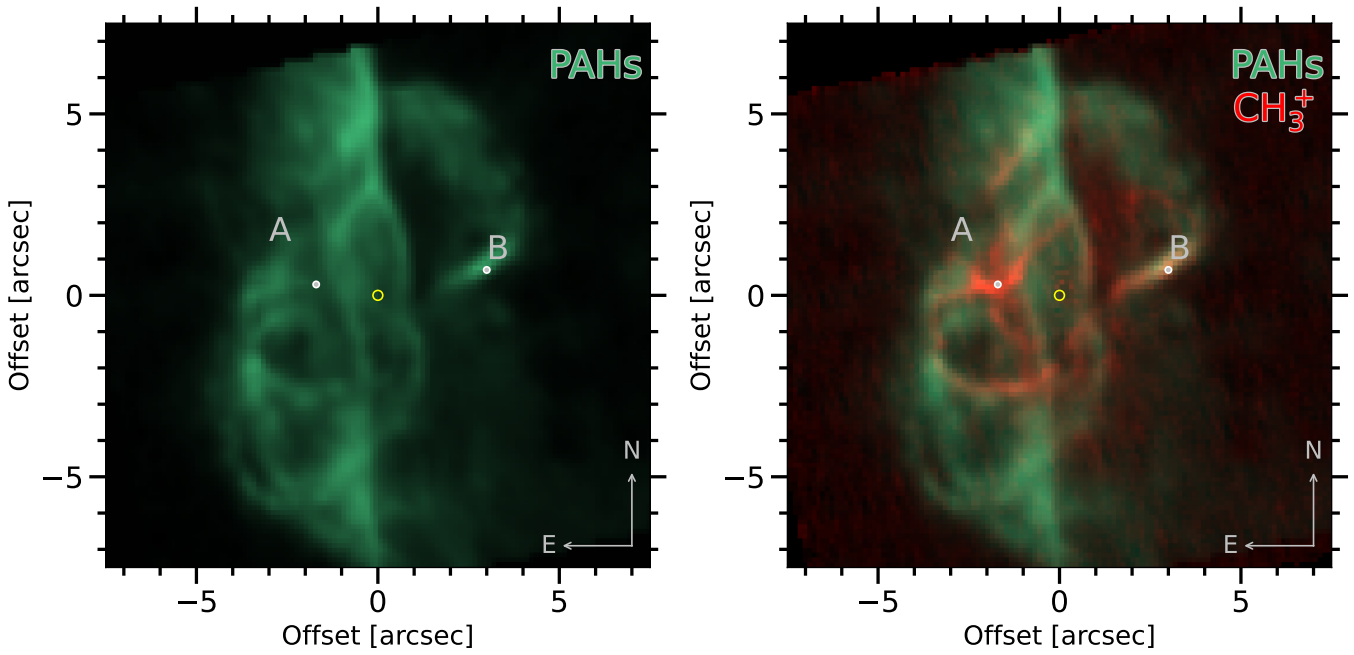

Figure 11. The PAH map (by Clark et al. 2025, in preparation) here on the left shows the integrated intensity of the 6.2 μm feature (integrated over the 6.12–6.5 μm range after continuum subtraction). A comparison with the CH_3^+ map is shown on the right. Locations marked by A and B represent the two bright spots on the CH_3^+ map. The maps are centered at the central star (R.A. = $17^h{:}13^m{;}44\overset{s}{.}488 \pm 0\overset{s}{.}004$, decl. = $-37°{:}06'{:}11\overset{''}{.}76 \pm 0\overset{''}{.}03$) whose position is indicated by the white circle at the center.

X-ray radiation can efficiently drive carbon chemistry in dense O-rich gas, where CH^+ and CH_3^+ can further react with e^-, C, and H_2 to form C_2H_2, which can then initiate the chemistry leading to aromatic species like PAHs if activation energies are overcome. Since PAH emission is widespread in NGC 6302's central region, including the torus, and inner and outer bubbles where CH_3^+ is detected, the role of CH_3^+ in the bottom-up PAH formation sequence should be investigated.

6. Summary and Conclusions

We report the detection of methyl cation (CH_3^+) in JWST-MIRI observations of the O-rich planetary nebula NGC 6302, marking the first identification of this key organic precursor in such an environment. We investigated the nature of the CH_3^+ emission and its relation to other species such as ^{12}CO, H_2, PAHs, and HCO^+. We fit the observed CH_3^+ emission with LTE models to derive excitation temperature and column density. Model fits reproduce the CH_3^+ emission very well, yielding excitation temperatures of 500–800 K in the inner bubble and the torus, significantly higher excitation temperature of 1000–2000 K in the outer bubble. Column densities of CH_3^+ in the excited state are typically $\sim 10^{12}$ cm^{-2}, ranging from $\sim 10^{11}$ cm^{-2} in the outer bubble to $\sim 10^{13}$ cm^{-2} where the inner bubble runs into the torus. These measurements represent only a fraction of the total population due to non-LTE chemical pumping. The spatial coincidence of CH_3^+ with ^{12}CO and H_2 supports its formation via chemical pumping in the UV-irradiated O-rich gas.

The presence of CH_3^+ in this O-rich PN highlights the carbon chemistry at play in O-rich environments under strong UV irradiation. These results indicate that hydrocarbon radical chemistry must be incorporated into chemical models of PNe. Further observations at comparable spatial resolution, particularly in the near-IR (which is rich in molecular features), are essential to unravel the different chemical networks involved in this chemistry.

Acknowledgments

This work is based on observations made with the NASA/ESA/CSA James Webb Space Telescope. All of the data presented in this article were obtained from the Mikulski Archive for Space Telescopes (MAST) at the Space Telescope Science Institute. The data of this specific observing program can be accessed via doi:10.17909/s1rn-1t84. This study is based on the international consortium of ESSENcE (Evolved Stars and their Nebulae in the JWST era). This article/publication is based upon work from COST Action NanoSpace, CA21126, supported by COST (European Cooperation in Science and Technology).

C.B., J.C., E.P., and N.C. acknowledge support from the University of Western Ontario, the Canadian Space Agency (CSA)[22JWGO1-22], and the Natural Sciences and Engineering Research Council of Canada. M.M. and R.W. acknowledge support from the STFC Consolidated grant (ST/W000830/1). M.J.B. and R.W. acknowledge support from the European Research Council (ERC) Advanced Grant SNDUST 694520. A.A.Z. acknowledges funding through UKRI/STFC through grant ST/T000414/1. H.L.D. acknowledges support from grant JWST-GO-01742.004 and NSF grants 1715332 and 2307117. N.C.S. acknowledges support from NSF award AST-2307116. G.G.-S. thanks Michael L. Norman and the Laboratory for Computational Astrophysics for the use of ZEUS-3D. The computations were performed at the Instituto de Astronomía-UNAM at Ensenada. P.J.K. acknowledges support from the Science Foundation Ireland/Irish Research Council Pathway program under grant No. 21/PATH-S/9360. R.S.'s contribution to the research described here was carried out at the Jet Propulsion Laboratory, California Institute of Technology, under a contract with NASA. K.E.K. acknowledges support from grant JWST-GO-01742.010-A. F.K. and

M.T. acknowledge support from the Spanish Ministry of Science, Innovation and Universities, under grant No. PID2023-149918NB-I00. This research was also partly supported by the Spanish program Unidad de Excelencia María de Maeztu CEX2020-001058-M, financed by MCIN/AEI/10.13039/501100011033. J.M.L. was supported by basic research funds of the Office of Naval Research.

Appendix A
Continuum

An example of the continuum adopted for fitting the CH_3^+ spectral features is shown in Figure 12.

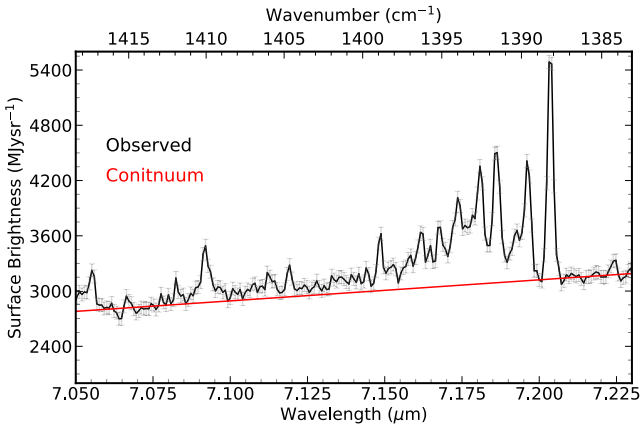

Figure 12. JWST MIRI spectrum at aperture 1 (in black). The red line provides an example of the continuum adopted to fit the models to the observations.

Appendix B
H_2 Map with Apertures

The 25 apertures used to sample the CH_3^+ emission across distinct regions are plotted on the H_2 map in Figure 13.

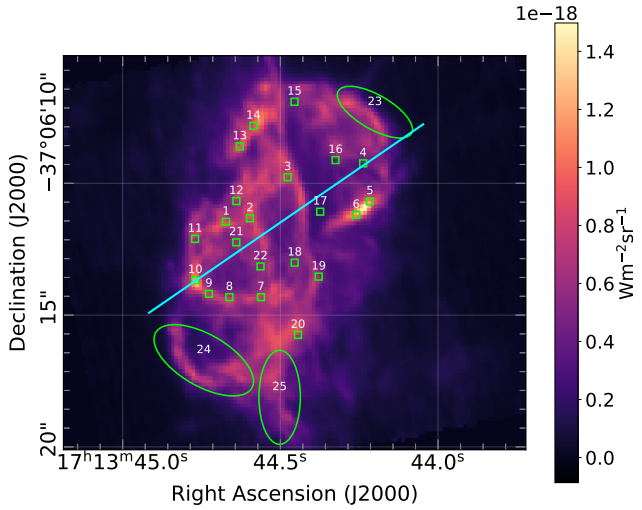

Figure 13. Integrated surface brightness map of H_2 0–0 S(5) line at 6.908 μm. The green boxes and ellipses represent the 25 apertures used to study CH_3^+ emission in detail.

Appendix C
Band Ratio Method

The best-fit Gaussians to the 7.15 and 7.2 μm bands for all 25 apertures are shown in Figures 14 and 15, respectively. These are used to determine the excitation temperature of CH_3^+ using the band ratio method as described in Section 4.

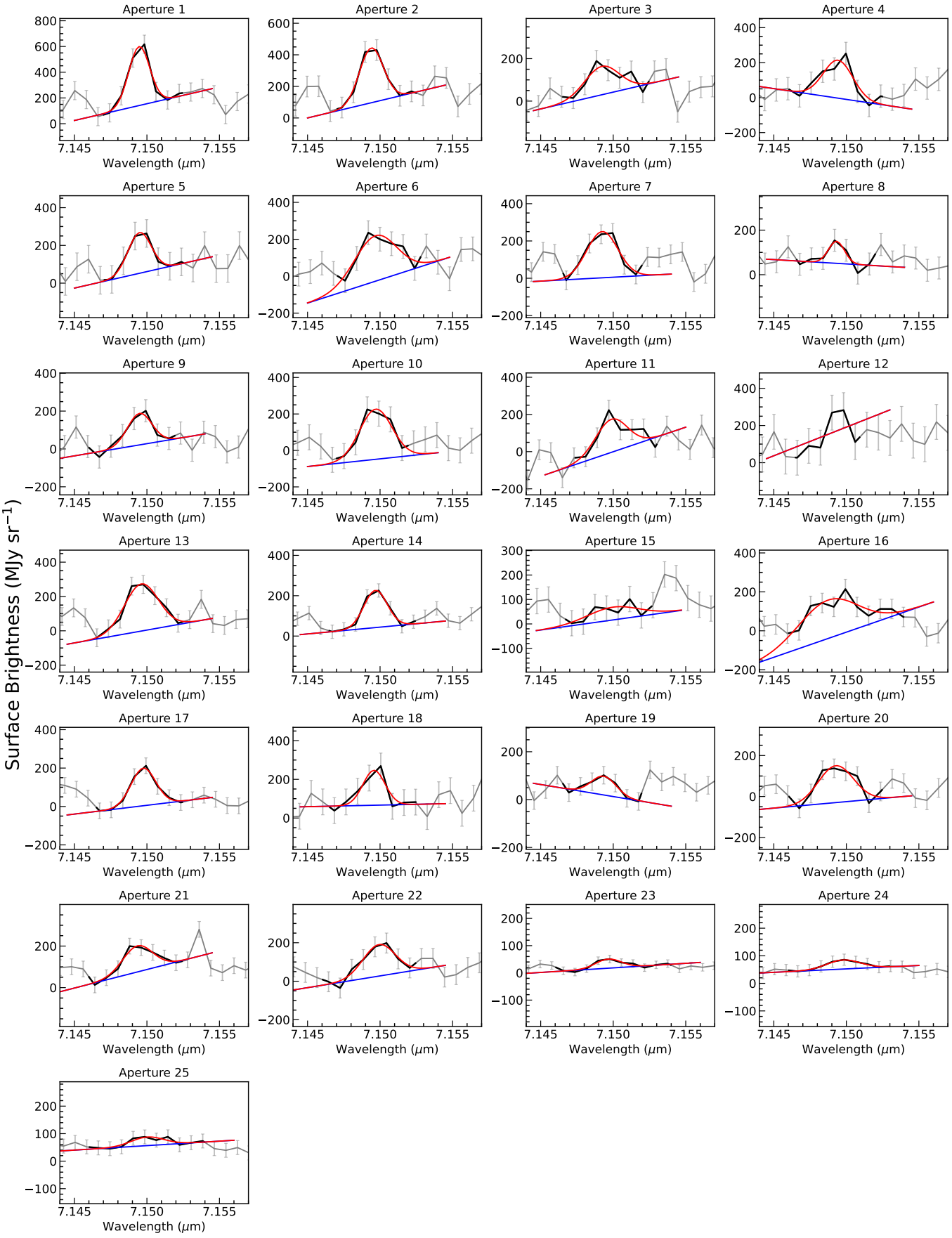

Figure 14. Gaussian fits to the 7.15 band used for the band ratio method to determine the temperature. The integrated surface brightness value at each aperture is listed in Table 1.

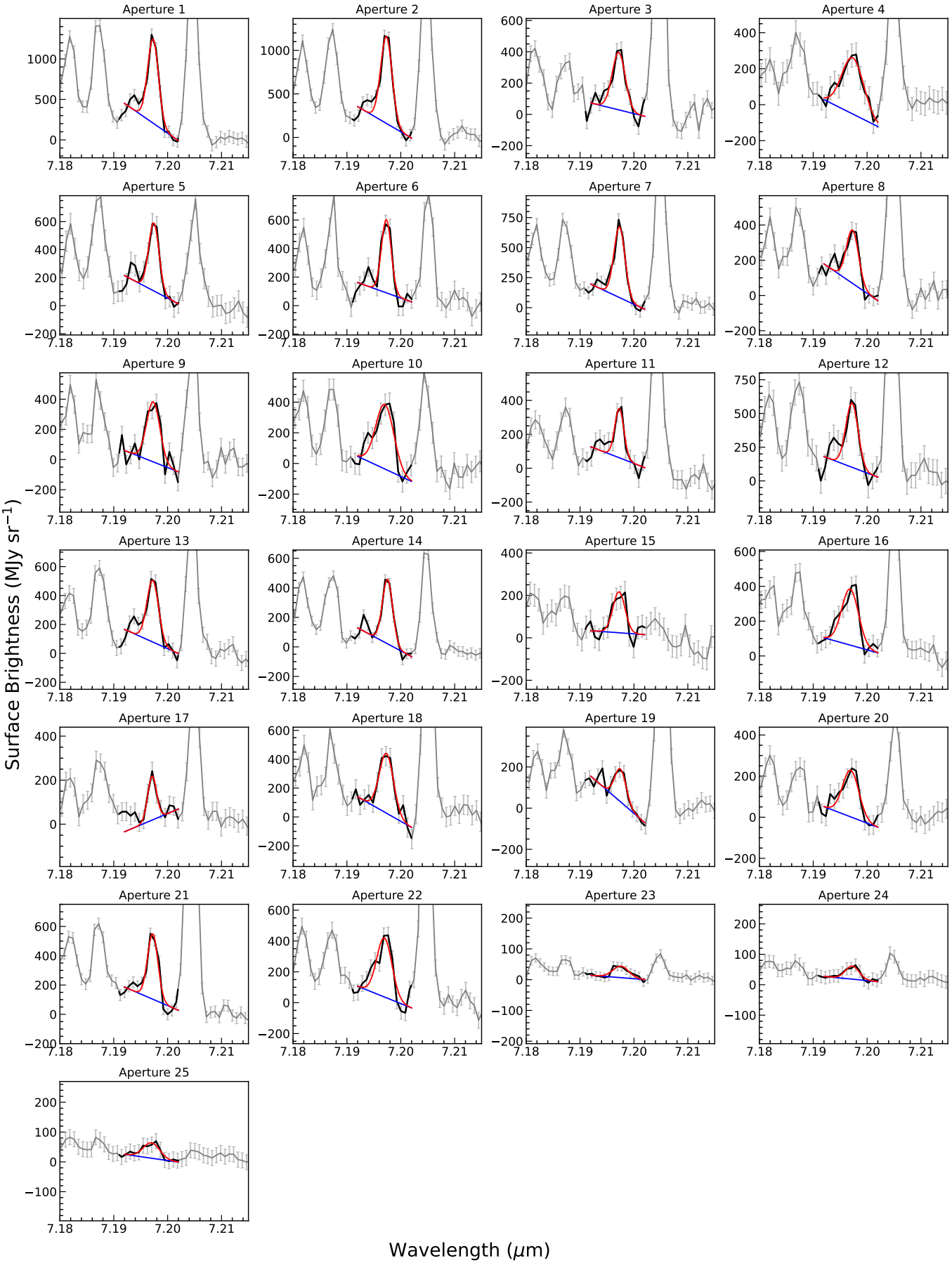

Figure 15. Gaussian fits to the 7.2 band used for the band ratio method to determine the temperature. The integrated surface brightness value at each aperture is listed in Table 1.

Appendix D
Fit Results

The best-fit models for determining CH_3^+ temperature and column density in all 25 apertures are shown in Figure 16. See Section 4 for details on the fitting procedure.

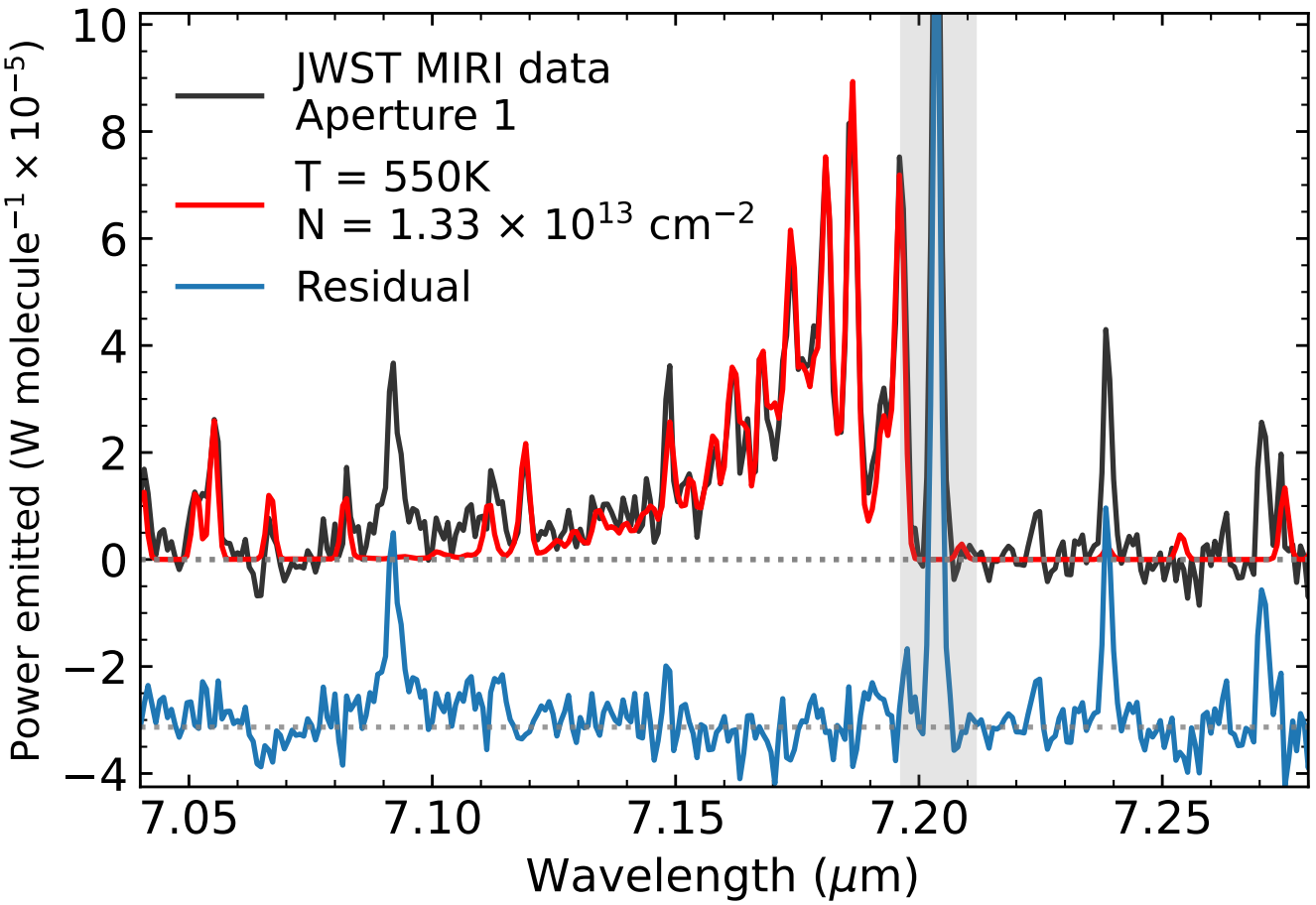

Figure 16. Observations (black), best-fit model (red), and residuals (blue) for aperture 1. The complete figure set for all 25 apertures is available. (The complete figure set (25 images) is available in the online article.)

ORCID iDs

Charmi Bhatt https://orcid.org/0009-0000-0191-6756
Jan Cami https://orcid.org/0000-0002-2666-9234
Els Peeters https://orcid.org/0000-0002-2541-1602
Paula Moraga Baez https://orcid.org/0000-0002-1042-235X
Kevin Volk https://orcid.org/0000-0002-3824-8832
Joel H. Kastner https://orcid.org/0000-0002-3138-8250
Harriet L. Dinerstein https://orcid.org/0000-0002-4017-5572
Mikako Matsuura https://orcid.org/0000-0002-5529-5593
Bruce Balick https://orcid.org/0000-0002-3139-3201
Kathleen E. Kraemer https://orcid.org/0000-0002-2626-7155
Kay Justtanont https://orcid.org/0000-0003-1689-9201
Olivia Jones https://orcid.org/0000-0003-4870-5547
Raghvendra Sahai https://orcid.org/0000-0002-6858-5063
Isabel Aleman https://orcid.org/0000-0002-7989-9041
Michael J. Barlow https://orcid.org/0000-0002-3875-1171
Joris Blommaert https://orcid.org/0000-0002-5797-2439
Naomi Hirano https://orcid.org/0000-0001-9304-7884
Patrick Kavanagh https://orcid.org/0000-0001-6872-2358
Francisca Kemper https://orcid.org/0000-0003-2743-8240
J. Martin Laming https://orcid.org/0000-0002-3362-7040
Hektor Monteiro https://orcid.org/0000-0002-0596-9115
Anita M. S. Richards https://orcid.org/0000-0002-3880-2450
N. C. Sterling https://orcid.org/0000-0002-9604-1434
Peter A. M. van Hoof https://orcid.org/0000-0001-7490-0739
L. B. F. M. Waters https://orcid.org/0000-0002-5462-9387
Roger Wesson https://orcid.org/0000-0002-4000-4394
Albert A. Zijlstra https://orcid.org/0000-0002-3171-5469

References

Agúndez, M. 2022, EPJWC, 265, 00029
Agúndez, M., Cernicharo, J., & Goicoechea, J. R. 2008, A&A, 483, 831
Agúndez, M., Cernicharo, J., & Guélin, M. 2014, A&A, 570, A45
Agúndez, M., Goicoechea, J. R., Cernicharo, J., Faure, A., & Roueff, E. 2010, ApJ, 713, 662
Araki, M. 2025, http://molecules-in.space/Molecules in Space—List of Observed Interstellar Molecules-đ
Argyriou, I., Glasse, A., Law, D. R., et al. 2023, A&A, 675, A111
Baez, M., Kastner, J.H., Bublitz, J., et al. 2025, Probing the Molecular Hearts of Extreme Bipolar Planetary Nebulae with ALMA, arXiv,
Balick, B., Borchert, L., Kastner, J. H., et al. 2023, ApJ, 957, 54
Berné, O., Martin-Drumel, M.-A., Schroetter, I., et al. 2023, Natur, 621, 56
Black, J. H., & Dalgarno, A. 1977, ApJS, 34, 405
Cami, J. 2002, PhD thesis, Univ. Amsterdam
Cami, J., Bernard-Salas, J., Peeters, E., & Malek, S. E. 2010, Sci, 329, 1180
Casassus, S., Roche, P. F., & Barlow, M. J. 2000, MNRAS, 314, 657
Changala, P. B., Chen, N. L., Le, H. L., et al. 2023, A&A, 680, A19
Cohen, M., Barlow, M. J., Liu, X. W., & Jones, A. F. 2002, MNRAS, 332, 879
Cox, N. L. J., Pilleri, P., Berné, O., Cernicharo, J., & Joblin, C. 2016, JPhCS, 728, 032011
De Beck, E., Kamiński, T., Patel, N. A., et al. 2013, A&A, 558, A132
Decin, L., De Beck, E., Brünken, S., et al. 2010, A&A, 516, A69
Decin, L., Richards, A. M. S., Danilovich, T., Homan, W., & Nuth, J. A. 2018, A&A, 615, A28
Feibelman, W. A. 2001, ApJ, 550, 785
García-Hernández, D. A., Zamora, O., Yagüe, A., et al. 2013, A&A, 555, L3
Godard, B., & Cernicharo, J. 2013, A&A, 550, A8
Gómez-Gordillo, S., Akras, S., Gonçalves, D. R., & Steffen, W. 2020, MNRAS, 492, 4097
Hasegawa, T. I., & Kwok, S. 2001, ApJ, 562, 824
Henning, T., Kamp, I., Samland, M., et al. 2024, PASP, 136, 054302
Herbst, E. 2021, FrASS, 8, 207
Höfner, S., & Olofsson, H. 2018, A&ARv, 26, 1
Kastner, J. H., Moraga Baez, P., Balick, B., et al. 2022, ApJ, 927, 100
Kim, H., Wyrowski, F., Menten, K. M., & Decin, L. 2010, A&A, 516, A68
Kwitter, K. B., & Henry, R. B. C. 2022, PASP, 134, 022001
Matsuura, M., Zijlstra, A. A., Molster, F. J., et al. 2005, MNRAS, 359, 383
Matsuura, M., Bernard-Salas, J., Lloyd Evans, T., et al. 2014, MNRAS, 439, 1472
Matsuura, M., Volk, K., Kavanagh, P., et al. 2025, The *JWST*/MIRI view of the planetary nebula NGC 6302 – I. A UV-irradiated torus and a hot bubble triggering PAH formation, Monthly Notices of the Royal Astronomical Society, 542, 1287
McGuire, B. A. 2022, ApJS, 259, 30
Meisner, J., Hallmen, P. P., Kästner, J., & Rauhut, G. 2019, JChPh, 150, 084306
Nagy, Z., Van der Tak, F. F. S., Ossenkopf, V., et al. 2013, A&A, 550, A96
Newville, M., Stensitzki, T., Allen, D. B., & Ingargiola, A. 2014, LMFIT: Non-Linear Least-Square Minimization and Curve-Fitting for Python, v0.8.0, Zenodo, doi:10.5281/zenodo.11813
Perea-Calderón, J. V., García-Hernández, D. A., García-Lario, P., Szczerba, R., & Bobrowsky, M. 2009, A&A, 495, L5
Peretto, N., Fuller, G., Zijlstra, A., & Patel, N. 2007, A&A, 473, 207
Posch, T., Kerschbaum, F., Mutschke, H., Dorschner, J., & Jäger, C. 2002, A&A, 393, L7
Santander-García, M., Bujarrabal, V., Alcolea, J., et al. 2017, A&A, 597, A27
Scott, G. B. I., Milligan, D. B., Fairley, D. A., Freeman, C. G., & McEwan, M. J. 2000, JChPh, 112, 4959
Smith, D. 1992, ChRv, 92, 1473
Stanghellini, L., García-Hernández, D. A., García-Lario, P., et al. 2012, ApJ, 753, 172
Sternberg, A., & Dalgarno, A. 1995, ApJS, 99, 565
Sylvester, R. J., Kemper, F., Barlow, M. J., et al. 1999, A&A, 352, 587
Tielens, A. G. G. M. 2013, RvMP, 85, 1021
Waters, L. B. F. M., Beintema, D. A., Zijlstra, A. A., et al. 1998a, A&A, 331, L61
Waters, L. B. F. M., Cami, J., de Jong, T., et al. 1998b, Natur, 391, 868
Wells, M., Pel, J. W., Glasse, A., et al. 2015, PASP, 127, 646
Western, C. M. 2017, JQSRT, 186, 221
Wright, N. J., Barlow, M. J., Ercolano, B., & Rauch, T. 2011, MNRAS, 418, 370
Zannese, M., Tabone, B., Habart, E., et al. 2025, A&A, 696, A99
Zhang, Y., & Kwok, S. 2011, ApJ, 730, 126
Zijlstra, A. A., Gaylard, M. J., te Lintel Hekkert, P., et al. 1991, A&A, 243, L9